Two mini-Neptunes transiting the adolescent K-star HIP 113103 confirmed with *TESS* and *CHEOPS*

N. Lowson [1]* G. Zhou,[1]* C. X. Huang,[1] D. J. Wright,[1] B. Edwards,[2] E. Nabbie,[1] A. Venner [1] S. N. Quinn,[3] K. A. Collins,[3] E. Gillen [4,5,6] M. Battley,[7] A. Triaud [8] C. Hellier,[9] S. Seager,[10,11,12] J. N. Winn,[13] J. M. Jenkins,[14] B. Wohler,[14,15] A. Shporer,[10] R. P. Schwarz,[3] F. Murgas,[16,17] E. Pallé,[16,17] D. R. Anderson [18,19] R. G. West [18,19] R. A. Wittenmyer,[1] B. P. Bowler,[20] J. Horner [1] S. R. Kane,[21] J. Kielkopf [22] P. Plavchan [23] H. Zhang,[24] T. Fairington,[1] J. Okumura,[1] M. W. Mengel [1] and B. C. Addison [1]

Affiliations are listed at the end of the paper

ABSTRACT

We report the discovery of two mini-Neptunes in near 2:1 resonance orbits (P = 7.610303 d for HIP 113103 b and P = 14.245651 d for HIP 113103 c) around the adolescent K-star HIP 113103 (TIC 121490076). The planet system was first identified from the *TESS* mission, and was confirmed via additional photometric and spectroscopic observations, including a ~17.5 h observation for the transits of both planets using ESA *CHEOPS*. We place ≤ 4.5 min and ≤ 2.5 min limits on the absence of transit timing variations over the 3 yr photometric baseline, allowing further constraints on the orbital eccentricities of the system beyond that available from the photometric transit duration alone. With a planetary radius of $R_p = 1.829^{+0.096}_{-0.067}$ $R_\oplus$, HIP 113103 b resides within the radius gap, and this might provide invaluable information on the formation disparities between super-Earths and mini-Neptunes. Given the larger radius $R_p = 2.40^{+0.10}_{-0.08}$ $R_\oplus$ for HIP 113103 c, and close proximity of both planets to HIP 113103, it is likely that HIP 113103 b might have lost (or is still losing) its primordial atmosphere. We therefore present simulated atmospheric transmission spectra of both planets using *JWST*, *HST*, and *Twinkle*. It demonstrates a potential metallicity difference (due to differences in their evolution) would be a challenge to detect if the atmospheres are in chemical equilibrium. As one of the brightest multi sub-Neptune planet systems suitable for atmosphere follow up, HIP 113103 b and HIP 113103 c could provide insight on planetary evolution for the sub-Neptune K-star population.

Key words: techniques: photometric – techniques: spectroscopic – planets and satellites: detection – stars: individual: TIC121490076.

1 INTRODUCTION

Super-Earths (1 $R_\oplus < R_p \leq 1.5$ $R_\oplus$) and mini-Neptunes (1.5 $R_\oplus < R_p \leq 4$ $R_\oplus$) are the most common planets found around sun-like stars (referred to as sub-Neptunes hereafter), especially those residing in close-in orbits (Howard et al. 2012; Fressin et al. 2013; Bergsten et al. 2022), despite having no analogues in our own Solar System. These planets bridge the gap between rocky Earth-like worlds and gaseous Neptunes (e.g. Fulton et al. 2017). The *Transiting Exoplanet Survey Satellite* (*TESS*; Ricker et al. 2015) mission continues to expand our repertoire for sub-Neptunes, in particular those orbiting bright nearby stars. These discoveries have led to precise radius and mass constraints for a significant number of sub-Neptunes (e.g. Dragomir et al. 2019; Gandolfi et al. 2019; Cloutier et al. 2020; MacDougall et al. 2021; Sozzetti et al. 2021; Gan et al. 2022; Lubin et al. 2022),

as well as the possibility of in-depth atmospheric characterizations that reveal the origins and evolutionary pathways of this population (e.g. Osborn et al. 2021; Kawauchi et al. 2022).

Hypothesized planet formation pathways for sub-Neptunes [see Bean, Raymond & Owen (2021) for more information] will exhibit observable differences that are accessible with the new generation of space and ground based facilities (e.g. Greene et al. 2016; Tinetti et al. 2018). Depending on what occurs after dissipation of the gas disc, sub-Neptunes may not contain enough mass to gravitationally maintain their primordial atmosphere (e.g. Walker 1986; Lopez, Fortney & Miller 2012; Ginzburg, Schlichting & Sari 2018; Kite & Barnett 2020; Kite et al. 2020). The rate of mass-loss post-formation is strongly dependent on the irradiation the planets receive from their host stars. Planets receiving strong XUV irradiation may be more likely to lose their primordial envelope (e.g. Owen & Jackson 2012; Howe & Burrows 2015; Mordasini 2020; Ketzer & Poppenhaeger 2022).

The next generation space-based telescopes [commencing with the *James Webb Space Telescope* (*JWST*); Greene et al. (2016)] will

be capable of characterizing the atmospheres of sub-Neptunes, and many are prioritizing wavelength regions towards the infrared (e.g. Tinetti et al. 2018; Stotesbury et al. 2022). Obstruction by haze and clouds are minimized at longer wavelengths, and early *JWST* observations have already demonstrated its invaluable retrieval capabilities for exoplanets atmospheres (e.g. Ahrer et al. 2023; Alderson et al. 2023; Feinstein et al. 2023; Rustamkulov et al. 2023; Tsai et al. 2023). Prior to the launch of these next generation telescopes, some attempts of measuring sub-Neptune atmospheres have resulted in observations obscured by haze (e.g. Kreidberg et al. 2014; Mugnai et al. 2021); however, there have been notable exceptions which suggest predominant H/He envelopes (e.g. Benneke et al. 2019; Tsiaras et al. 2019; Edwards et al. 2022; Orell-Miquel et al. 2022). Due to their size, observing sub-Neptune atmospheres is challenging in comparison to their larger Jovian counterparts, particularly around FGK stars. Therefore, the most suitable population of sub-Neptunes for atmosphere analysis are those residing in close orbits to bright host stars. In the known FGK planet population, there are only a handful of sub-Neptunes that meet these requirements (e.g. Winn et al. 2011; Gandolfi et al. 2018; Dragomir et al. 2019; Teske et al. 2020), with samples dwindling further when only considering multisub-Neptune planet systems (e.g. Rodriguez et al. 2018; Delrez et al. 2021; Scarsdale et al. 2021; Barragán et al. 2022). It is therefore vital to identify sub-Neptunes with short periods around bright stars, as these candidates will lead the research towards understanding the formation pathways of this vast sub-class.

In this paper, we report the discovery of two sub-Neptunes that orbit at a 2:1 resonance around the bright K-star HIP 113103 (TIC 121490076). The initial observations with *TESS* and subsequent follow up with the *CHaracterising ExOPlanets Satellite* (*CHEOPS*; Benz et al. 2021) and ground-based facilities are outlined in Section 2, while our global model fit to constrain the physical parameters of each planet are outlined in Section 3. The physical properties of HIP 113103 are discussed in Section 4, while the elimination of false positive scenarios are outlined in Section 5. Our Results and Discussion are presented in Section 6 followed by our Conclusion in Section 7, respectively.

2 OBSERVATIONS

2.1 Candidate identification with *TESS*

The transiting planets around HIP 113103 were first identified by observations from *TESS*. Observations for HIP 113103 were obtained via the 30 min cadence Full Frame Images (FFI) from Sector 1 Camera 2, and via 10 min FFIs and 2 min target pixel stamps from Sector 28 Camera 2.

The transit signals around HIP 113103 were identified as part of a search for planets around young active field stars (Zhou et al. 2021) via public FFI light curves from the MIT Quick look pipeline (Huang et al. 2020a, b). The target star was identified as a potential young star via its high amplitude rotational modulation using the 10 min FFI light curves from Sector 28. The combined FFI light curves of Sector 1 and 28 were first modeled and detrended via a spline interpolation (Vanderburg & Johnson 2014), and searched for transit signals via the box-least-squared (BLS) procedure (Kovács, Zucker & Mazeh 2002). Two candidate signals are detected by BLS, one at ≈ 7.61 d with a signal to noise of 14, the other at ≈ 14.24 d with a signal to noise of 12.79. Both signals crossed the recommended threshold to be classified as a threshold crossing event (TCE) as defined by the *TESS* Objects of Interest (TOI) team (Guerrero et al. 2021). We vetted the data for both TCEs to rule out astrophysical false positives

due to blending from nearby eclipsing binaries outside of the centre pixel. We found that transit depth derived from different apertures are similar, and found no obvious blending sources when examining light curves from individual pixels in and around the aperture. We then promoted both TCEs for further follow up via *CHEOPS* (Section 2.2) and ground based instruments (Sections 2.3 and 2.4).

To refine the orbital and physical characteristics of the planets in our global model (Section 3), we use of the debelended Sector 28 target pixel stamp (TPF) 2-min cadence Simple Aperture Photometry (SAP) light curves (Twicken et al. 2010; Morris et al. 2020), performing the deblending using the contamination keywords in the TPF files. These light curves originate from the Science Processing Operations Center (SPOC; Jenkins et al. 2016) at NASA Ames Research Center, and are made available via the the Mikulski Archive for Space Telescopes (MAST).[1] HIP 113103 exhibits significant rotational modulation due to spot activity on the stellar surface. To ensure proper propagation of the uncertainties associated with these noise sources, we model the rotational modulation and spacecraft systematics alongside the transiting planet signals. We use the deblended simple aperture SPOC light curves in this simultaneously detrending procedure. Following Vanderburg et al. (2019), we describe these signals as a linear combination of the spacecraft quaternions, the top seven covariant basis vectors, and a set of 20 cosine and sine functions at frequencies up to the *TESS* orbital period of 13 d (also see Mazeh & Faigler 2010; Huang, Bakos & Hartman 2013). Fig. 1 shows the *TESS* discovery light curve before and after the removal of the stellar and instrumental effects, while Fig. 2 and Fig. 3, 3, 4 show the individual transit light curves centred at HIP 113103 b and HIP 113103 c respectively. Fig. 4 shows the phase folded *TESS* transit light curves for each planet.

2.2 *CHEOPS* follow-up photometry

Although we detected HIP 113103 b and HIP 113103 c through *TESS*, additional observations with higher precision are required to confirm and constrain the radius and ephemerides values for both planets. We therefore use the *CHEOPS* mission to observe the primary transit of both planets during a single observing window. *CHEOPS* is a visible to infrared (0.4 μm − 1.1 μm) 0.32-m Ritchey–Chretien telescope located in a 700-km geocentric Sun-synchronous orbit. It is capable of capturing high-precision photometry of exoplanets around bright stars, with the corresponding *CHEOPS* mission focusing on the radius refinement of super-Earths and sub-Neptunes (Benz et al. 2021).

The *CHEOPS* observation (observation ID: 1901592) was obtained between 2022 September 9 20:31 and 2022 September 10 14:06 UTC (10 orbits over ∼17.5 h), with a ∼5 h baseline between ingress and egress of both transits. At an exposure time of 60 s, 700 frames are obtained, with 10 frames affected by stray light and Earth occultation. This observation of a near-simultaneous transit for HIP 113103 b and HIP 113103 c was possible only because of the near 2:1 resonance of the system.

The low Earth orbit nadir-locked orientation of *CHEOPS* naturally induces field rotation over the course of a spacecraft-orbit, and results in correlated systematics in the observed light curve. We modelled these effects alongside the transit model as part of our global modelling (Section 3). The spacecraft signals are modelled as a linear combination of the sky background, smear, contamination, pixel X and Y drifts, and a set of four sine and cosine functions at

---

[1] https://archive.stsci.edu/
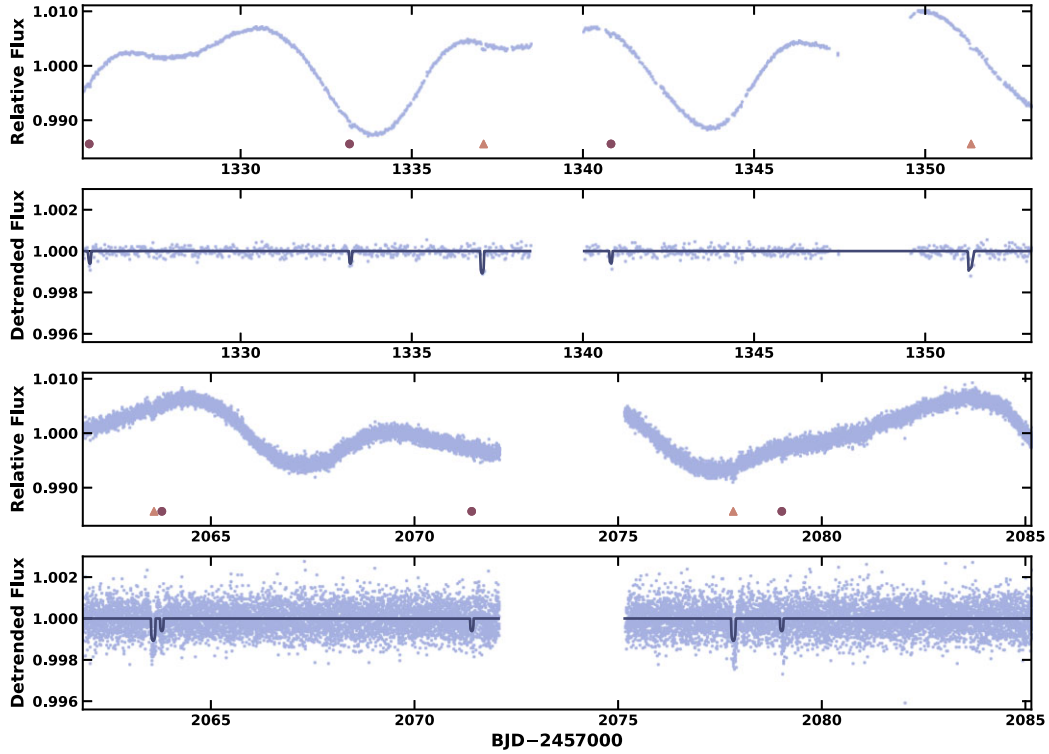
Figure 1. The *TESS* light curves before and after the removal of spot modulated rotational signals. The light curves of HIP 113103 from Sector 1 via FFI observations were observed at 30 min cadence (Panels 1 and 2), and from Sector 28 TPF observations at 2 min (Panels 3 and 4). Transits by HIP 113103 b and HIP 113103 c are illustrated via a circle and triangle respectively. The best-fitting transit model is displayed in navy.
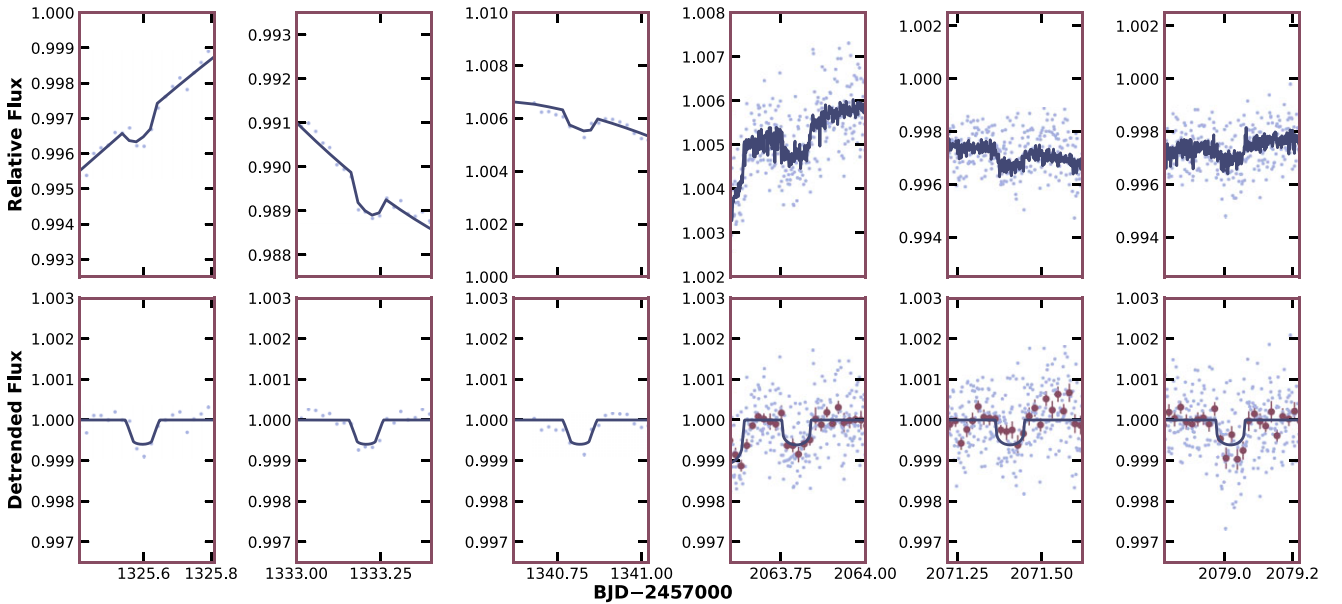
Figure 2. The *TESS* light curves centred on the transits of HIP 113103 b. The top panel shows the pre-detrending, the bottom panel shows the post-detrending light curves, after the removal of spot modulated rotational signal from HIP 113103. Columns 1–3 were observed at 30-min cadence during Sector 1, while 4–6 were observed at 2-min cadence from Sector 28. The best-fitting transit model is displayed in navy, and the detrended transits at 2-min cadence have been binned in 10-min intervals to illustrate the precision of *TESS*.
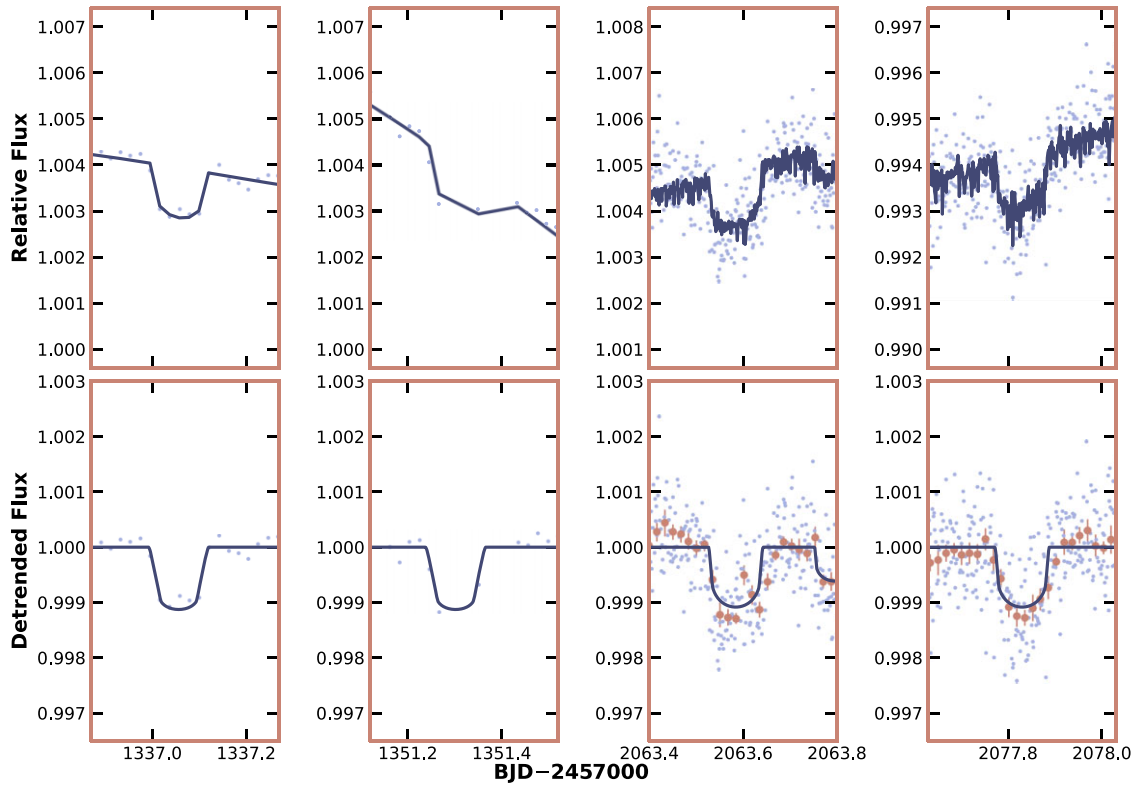
Figure 3. The *TESS* light curves centred on the transits of HIP 113103 c. The top panel shows the pre-detrending, the bottom shows the post-detrending light curve, after the removal of spot modulated rotational signal from HIP 113103. Columns 1–2 were observed at 30-min cadence during Sector 1, while 3–4 were observed at 2-min cadence during Sector 28. The best-fitting transit model is displayed in navy, and the detrended transits at 2-min cadence have been binned in 10-min intervals to illustrate the precision of *TESS*.
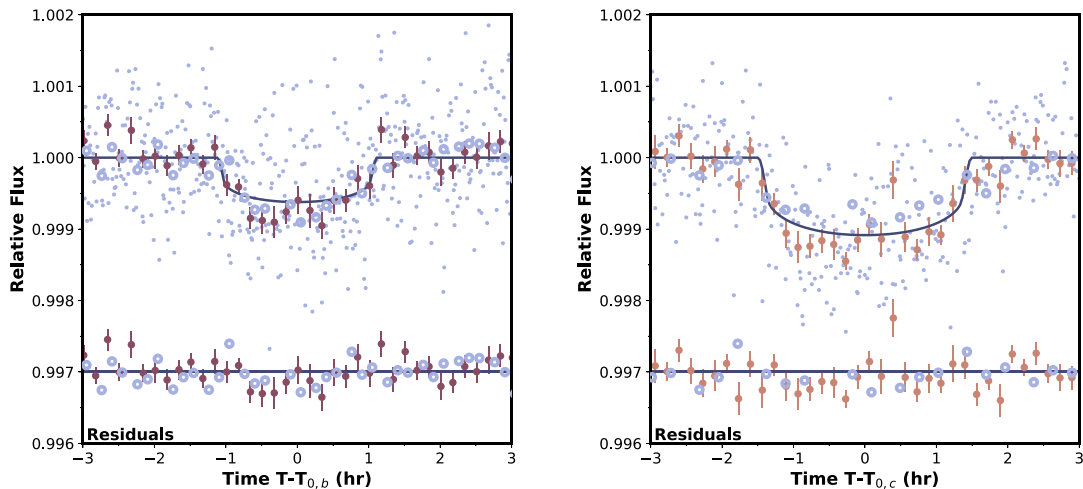

Figure 4. Phase folded *TESS* transit light curves for HIP 113103 b (left) and HIP 113103 c (right). The light blue open circles represent 30-min cadenced observations, while the light blue filled points represent the 2-min cadenced observations. The points with error bars show the binned 2-min light curves at 10-min cadence. The best-fitting models are over plotted. The binned residuals are plotted at the bottom, vertically offset by 0.003 in flux for clarity.

frequencies up to four times the spacecraft orbital period as a function of the spacecraft roll angle.

Fig.5 shows the raw and detrended *CHEOPS* light curves, and the model describing the instrumental signals that were removed from the raw light curve.

2.3 Ground-based follow-up photometry

In addition to space-based observations, we also obtained ground-based seeing limited photometry through the *TESS* Follow-up Observing Program (TFOP) photometry science working group (SG1)
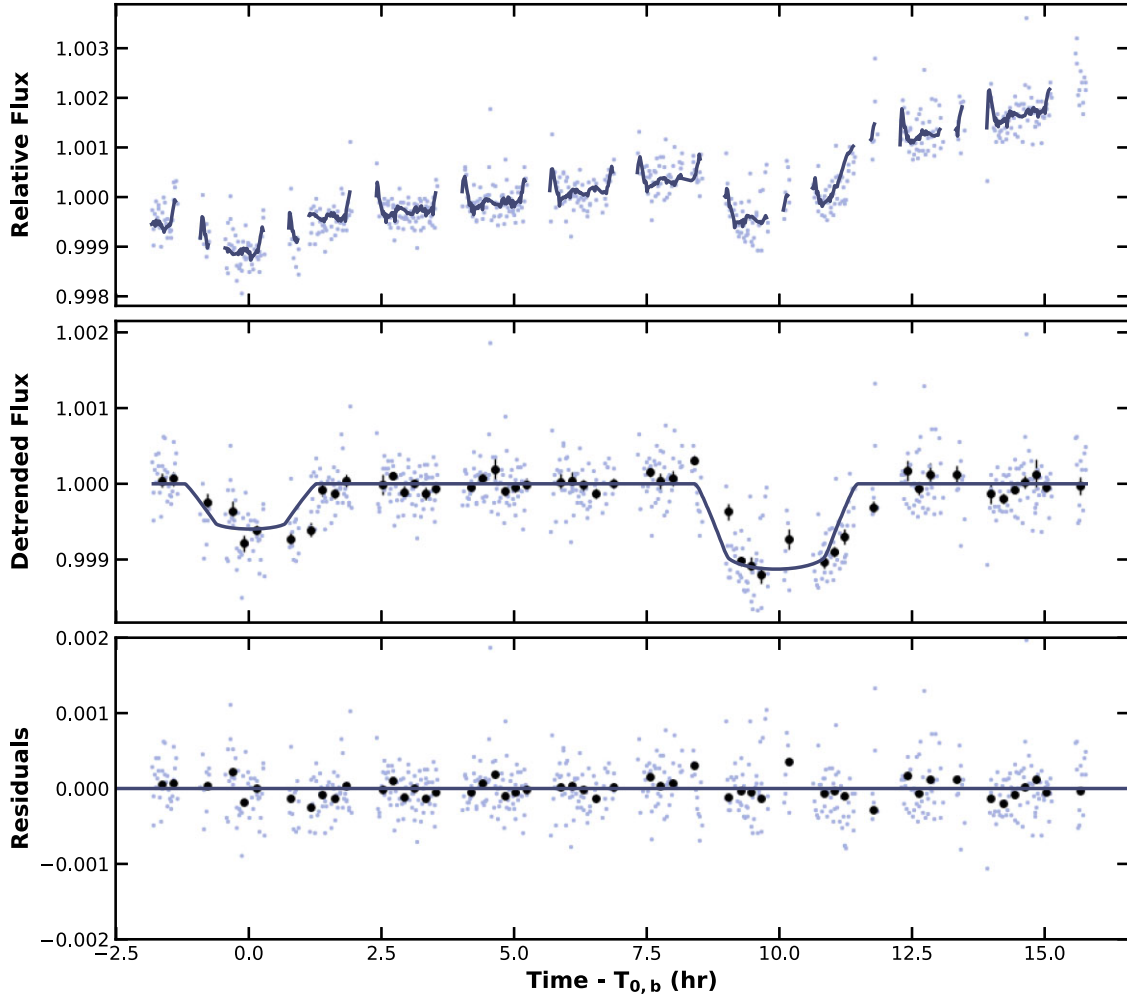
Figure 5. The follow-up *CHEOPS* observations of HIP 113103 b (first transit) and HIP 113103 c (second transit) taken over a single ∼17.5 h visit. The top panel displays the raw light curves from the optimal aperture extraction. The model describing the planetary transits and the instrumental effects is overplotted via the navy line (see Section 3). The middle panel shows the detrended *CHEOPS* light curve after removal of the instrumental spacecraft orbit induced variations and the best-fitting transit model. The transits are binned in 10-min intervals to illustrate the precision of *CHEOPS*. The bottom panel illustrates the residuals of the data.

to detect the transits of both planets and further rule out other nearby targets contaminating the detection.

Two transits of both HIP 113103 b and HIP 113103 c were obtained using the Las Cumbres Observatory Global Telescope (LCOGT Brown et al. 2013) facility. We used the 1-m telescopes of the LCOGT network for these observations. Each telescope is equipped with a *sinistro* 4 K × 4 K andor EM CCD camera, yielding a field of view of 5.7 arcmin and a pixel scale of 0.34″ pixel⁻¹. These observations are able to detect the transits of both planets with high significance, and determine that the transit depths are consistent with those derived from *TESS* and *CHEOPS*. The images were calibrated using the standard LCOGT ʙᴀɴᴢᴀɪ pipeline (McCully et al. 2018) and the differential photometric data was extracted using ᴀsᴛʀᴏɪᴍᴀɢᴇᴊ (Collins et al. 2017). Given *Gaia* DR3 catalogue shows that no other stars are within 10 arcsec of HIP 113103, we determine that the transit signals most likely originated from the target star. The light curves are detrended simultaneously against the airmass in our global fit. Fig. 6 shows the detrended light curves against their respective model light curve from our global model fit. The observations are detailed as follows:

A full transit of HIP 113103 b was obtained via the 1-m telescope at the South African Astronomical Observatory (SAAO) on UT 2022-09-09 with a 5.5 arcsec radius aperture using the z_s filter. On UT 2022-09-10, a partial transit of HIP 113103 c, including ingress, was obtained from the Cerro Tololo Interamerican Observatory (CTIO) node with a 6.2 arcsec radius aperture using the z_s filter. An additional full transit for both HIP 113103 b and HIP 113103 c were obtained from the *CTIO* node on UT 2022-09-10 and UT 2022-10-22. Both transits were obtained with the z_s filter, with an aperture size of 8.2 arcsec and 7.0 arcsec for HIP 113103 b and HIP 113103 c, respectively. Table 1 displays all the photometric transit observations analysed in this work.

2.4 Spectroscopic characterization

To characterize the stellar properties of the host star and validate the planetary-nature of the transiting candidates, we obtained a series of reconnaissance spectroscopic observations of HIP 113103 with a set of southern spectroscopic facilities.
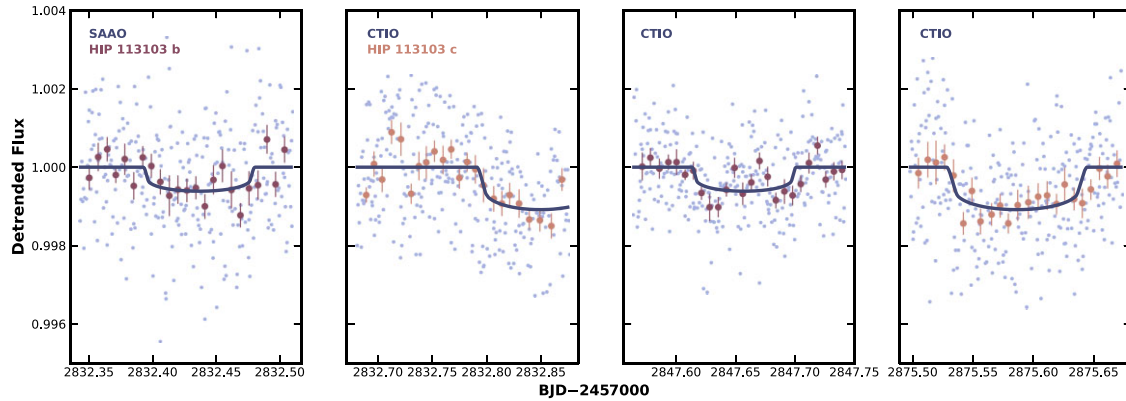
Figure 6. The ground-based detrended photometric follow-up observations of HIP 113103 b and HIP 113103 c, as obtained with the Las Cumbres Observatory 1-m telescopes at the South African Astronomical Observatory and the Cerro Tololo Interamerican Observatory (all in z_s filter). The best-fitting transit model is represented via the navy line, while each transit has been binned in 10-min intervals to illustrate the precision of the *LCO* telescopes.

Table 1. A summary of all ground-based photometric transit observations for HIP 113103 b and HIP 113103 c.

Target	Instrument	Date (UT)	Filter	Aperture
HIP 113103 b	SAAO 1.0 m	2022-09-09	z_s	5.5 arcmin
HIP 113103 c	CTIO 1.0 m	2022-09-10	z_s	6.2 arcmin
HIP 113103 b	CTIO 1.0 m	2022-09-25	z_s	8.2 arcmin
HIP 113103 c	CTIO 1.0 m	2022-10-22	z_s	7.0 arcmin

These instruments are involved in the LCOGT consortium.

Table 2. Radial velocity measurements of HIP 113103.

BJD	RV (km s^{-1})	σ_{RV} (km s^{-1})	Instrument
2459171.60440	12.813	0.035	CHIRON
2459174.59126	12.864	0.024	CHIRON
2459176.58998	12.824	0.022	CHIRON
2459178.62741	12.858	0.026	CHIRON
2459180.55586	12.818	0.029	CHIRON
2459182.53304	12.830	0.034	CHIRON
2459184.55875	12.854	0.026	CHIRON
2459186.62126	12.877	0.022	CHIRON
2459917.93684	13.370	0.022	MINERVA-Australis
2459917.95510	13.425	0.019	MINERVA-Australis
2459924.93091	13.377	0.015	MINERVA-Australis
2459924.94916	13.382	0.020	MINERVA-Australis
2459930.93397	13.356	0.038	MINERVA-Australis
2459930.95226	13.406	0.020	MINERVA-Australis
2459942.92801	13.384	0.019	MINERVA-Australis
2459942.94630	13.407	0.018	MINERVA-Australis
2460046.29239	13.435	0.035	MINERVA-Australis
2460046.31065	13.409	0.014	MINERVA-Australis

The stellar atmospheric parameters were derived by matching each observation against a library of $\sim$10 000 observed spectra previously classified through the Spectroscopic Classification Pipeline (Buchhave et al. 2012). The library is interpolated via a gradient boosting regressor model, from which the best-fitting spectral parameters were determined (Zhou et al. 2021). We found a best-fitting effective temperature of $T_{\mathrm{eff}} = 4930 \pm 100$ K, surface gravity of $\log g = 4.6 \pm 0.1$ dex, metallicity of [m/H] $= -0.1 \pm 0.1$ dex, and projected rotational broadening of $v \sin I_\star = 3 \pm 1 \,\mathrm{km\,s^{-1}}$ for HIP 113103. We note that the rotational velocity is less than the instrument broadening, and the reported value is likely an upper limit of the true rotation velocity.

In addition, we obtained eight observations of HIP 113103 using the CHIRON facility on the SMARTS 1.5-m telescope located at Cerro Tololo Inter-American Observatory, Chile (Tokovinin et al. 2013). CHIRON is a fibre-fed echelle spectrograph with a resolving power of $R \sim 80\,000$ over the wavelength range of 4100–8700 Å. We use the extracted spectra from CHIRON reduced via the standard pipeline as per Paredes et al. (2021). The radial velocities are derived from each observation via a least-squares deconvolution of the spectra against a synthetic template generated at the atmospheric parameters of the target star (Donati et al. 1997). The generated line profiles are modelled via a combination of kernels describing the rotational, macroturbulent, and instrument broadening effects (following Gray & Corbally 1994).

We also obtained 10 epochs of spectroscopic observations from the MINERVA-Australis array. MINERVA-Australis is an array of four identical 0.7-m telescopes, located at Mt Kent Observatory, Australia. The light from all four telescopes are combined into a single KIWISPEC high resolution echelle spectrograph, with a resolving power of $R \sim 80\,000$ over the wavelength region of 4800–6200 Å (Barnes et al. 2012; Addison et al. 2019). Wavelength corrections are provided by

two simultaneous fibers adjacent to the object fibers, which pass light from a quartz lamp through an iodine cell. Relative radial velocities are derived by a cross correlation between each individual observation and an averaged spectrum of the set of spectra available for the target. These relative velocities are then shifted to the mean absolute velocity of the averaged spectrum. These velocities are also presented in Table 2.

The MINERVA-Australis observations have per-point uncertainties of 10–20 m s^{-1}, and are comparable to those obtained from CHIRON. We do not detect significant radial velocity variations at the 20 m s^{-1} level, consistent with the expected low mass of the planets around HIP 113103. The observations therefore remain consistent with a lack of detection of the radial velocity orbit, as is expected given the velocity uncertainties and the expected orbit amplitude. The line profiles exhibit no visible variations indicative of blend scenarios. In scenarios where the transit is induced by a background eclipsing binary, we would often observe correlations between the rotational broadening velocity and the radial velocities, with the apparent broadening at its maximum at the extremities of the velocity curve. We observe no such correlation for HIP 113103, with the exposure to exposure scatter in the rotational broadening of 0.2 km s^{-1}.

Table 3. The physical properties of HIP 113103.

Parameter	Value	Source
Identifiers	HIP 113 103	
	TIC 121 490 076	
	TYC 8011-00766-1	
	2MASS J22541736-4300372	
	Gaia DR2 6 541 360 574 788 758 016	
Astrometry		
RA	$22^h54^m17^s.37$	Gaia Collaboration (2022)
Dec.	$-43°00'37''.25$	Gaia Collaboration (2022)
Parallax (mas)	21.61785 ± 0.00024	Gaia Collaboration (2022)
Proper motion		
Gaia (2016.4) RA proper motion (mas yr^{-1})	1.995 ± 0.020	Gaia Collaboration (2022)
Gaia (2016.3) Dec. proper motion (mas yr^{-1})	27.384 ± 0.021	Gaia Collaboration (2022)
Hipparcos (1991.2) RA proper motion (mas yr^{-1})	2.2 ± 1.5	Perryman et al. (1997)
Hipparcos (1991.4) Dec. proper motion (mas yr^{-1})	27.1 ± 1.3	Perryman et al. (1997)
Hipparcos-Gaia average RA proper motion (mas yr^{-1})	2.032 ± 0.048	Brandt (2021)
Hipparcos-Gaia average Dec. proper motion (mas yr^{-1})	27.396 ± 0.038	Brandt (2021)
Photometry		
TESS (mag)	8.9988 ± 0.0063	Stassun et al. (2019)
B (mag)	10.907 ± 0.033	Høg et al. (2000)
V (mag)	9.95 ± 0.03	Høg et al. (2000)
J (mag)	8.195 ± 0.03	Skrutskie et al. (2006)
H (mag)	7.67 ± 0.042	Skrutskie et al. (2006)
K (mag)	7.557 ± 0.031	Skrutskie et al. (2006)
Gaia G (mag)	9.6175 ± 0.0018	Gaia Collaboration (2022)
Gaia$_{BP}$ (mag)	10.1491 ± 0.0033	Gaia Collaboration (2022)
Gaia$_{RP}$ (mag)	8.9353 ± 0.0039	Gaia Collaboration (2022)
WISE W1 (mag)	7.398 ± 0.033	Cutri & et al. (2012)
WISE W2 (mag)	7.538 ± 0.02	Cutri & et al. (2012)
WISE W3 (mag)	7.489 ± 0.017	Cutri & et al. (2012)
WISE W4 (mag)	7.395 ± 0.132	Cutri & et al. (2012)
Kinematics and position		
U (km s^{-1})	5.00 ± 0.17	Propagated from Gaia[1]
V (km s^{-1})	4.635 ± 0.031	Propagated from Gaia[1]
W (km s^{-1})	-13.89 ± 0.32	Propagated from Gaia[1]
Distance (pc)	46.212 ± 0.086	This paper
$\gamma_{\rm CHIRON}$ (km s^{-1})	$12.845^{+0.012}_{-0.013}$	This paper
$\gamma_{\rm MINERVA}$ (km s^{-1})	$13.395^{+0.010}_{-0.011}$	This paper
Jitter$_{\rm CHIRON}$ (m s^{-1})	16^{+20}_{-11}	This paper
Jitter$_{\rm MINERVA}$ (m s^{-1})	13^{+14}_{-9}	This paper
Physical properties		
$M_\star$ (M$_\odot$)	0.761 ± 0.038	This paper
$R_\star$ (R$_\odot$)	0.742 ± 0.013	This paper
$T_{\rm eff}$ (K)	4930 ± 100	This paper
$\log g$ (cgs)	4.6 ± 0.1	This paper
[m/H]	-0.1 ± 0.1	This paper
$v\sin i$ (km s^{-1})	3 ± 1	This paper
Rotation period (d)	9.92 ± 0.23	This paper
Gyrochronology age (Myr)	470^{+170}_{-110}	Based on the gyrochronology relationship from Bouma, Palumbo & Hillenbrand (2023)
Limb darkening coefficients (*TESS*$_{u1}$)	0.463 ± 0.021	Claret (2017)
Limb darkening coefficients (*TESS*$_{u2}$)	0.182 ± 0.020	Claret (2017)
Limb darkening coefficients (*CHEOPS*$_{u1}$)	0.604 ± 0.021	Claret & Bloemen (2011)
Limb darkening coefficients (*CHEOPS*$_{u2}$)	0.111 ± 0.022	Claret & Bloemen (2011)
Limb darkening coefficients (LCO z' band $_{u1}$)	0.350 ± 0.021	Claret & Bloemen (2011)
Limb darkening coefficients (LCO z' band $_{u2}$)	0.287 ± 0.021	Claret & Bloemen (2011)

[1] Propagated from *Gaia* via the GAL UVW function in the PYASTRONOMY package (Czesla et al. 2019).

In addition, two archival spectra were obtained from the European Southern Observatory (ESO) HARPS facility on the ESO 3.6-m telescope in La Silla, Chile (Mayor et al. 2003). The observations have a spectral resolution of $R = 120\,000$ over the spectral range of 3780–6910 Å. We make use of the two archival observations, obtained in 2010 and 2013, to further classify the host star atmospheric properties. To calculate the spectroscopic parameters, we make use of the ZASPE package (Brahm et al. 2017) and its associated

Table 4. Derived parameters for HIP 113 103 b and HIP 113 103 c.

Parameter	Value	Prior
Fitted parameters for HIP 113103 b		
T_0 (BJD-TDB)	$1325.5966^{+0.0033}_{-0.0024}$	Fitted
P (days)	7.610303 ± 0.000018	Fitted
$R_p/R_\star$ ($R_\star$)	$0.0242^{+0.0013}_{-0.0008}$	Fitted
i (deg)	$88.23^{+0.18}_{-0.14}$	Fitted
$\sqrt{e}\cos\omega$	$0.18^{+0.51}_{-0.45}$	Fitted
$\sqrt{e}\sin\omega$	$-0.12^{+0.31}_{-0.32}$	Fitted
Inferred parameters for HIP 113103 b		
e	$0.17^{+0.17}_{-0.13}$	Derived
ω (deg)	-10^{+120}_{-140}	Derived
R_p ($R_\oplus$)	$1.829^{+0.096}_{-0.067}$	Derived
$a/R_\star$ ($R_\star$)	$21.39^{+0.10}_{-0.13}$	Derived
a (au)	$0.06899^{+0.00029}_{-0.00023}$	Derived
T_{14} (days)	$0.0891^{+0.0075}_{-0.0068}$	Derived
T_{eq} (K)	721 ± 10	Derived
b	$0.656^{+0.070}_{-0.084}$	Derived
$(R_p/R_\star)^2$	$0.000596^{+0.000062}_{-0.000051}$	Derived
M_p ($M_\oplus$) from mass–radius relationships	$5.9 \pm 1.9^*$	Inferred
K_{RV} (m s^{-1}) from mass–radius relationships	$2.34 \pm 0.73^*$	Inferred
ρ_p ($\rho_\oplus$) from mass–radius relationships	$0.96^{+0.15}_{-0.22}$ *	Inferred
Fitted parameters for HIP 113103 c		
T_0 (BJD-TDB)	1337.0559 ± 0.0019	Fitted
P (days)	14.245648 ± 0.000019	Fitted
$R_p/R_\star$ ($R_\star$)	$0.0303^{+0.0014}_{-0.0010}$	Fitted
i (deg)	$89.24^{+0.40}_{-0.22}$	Fitted
$\sqrt{e}\cos\omega$	$-0.31^{+0.23}_{-0.25}$	Fitted
$\sqrt{e}\sin\omega$	$0.21^{+0.13}_{-0.18}$	Fitted
Inferred parameters for HIP 113103 c		
e	$0.17^{+0.17}_{-0.13}$	Derived
ω (deg)	-70^{+100}_{-60}	Derived
R_p ($R_\oplus$)	$2.40^{+0.10}_{-0.08}$	Derived
$a/R_\star$ ($R_\star$)	$32.49^{+0.15}_{-0.19}$	Derived
a (au)	$0.10479^{+0.00045}_{-0.00035}$	Derived
T_{14} (days)	$0.1764^{+0.0091}_{-0.0050}$	Derived
T_{eq} (K)	585 ± 10	Derived
b	$0.614^{+0.028}_{-0.063}$	Derived
$(R_p/R_\star)^2$	$0.001051^{+0.00011}_{-0.000087}$	Derived
M_p ($M_\oplus$) from mass–radius relationships	$8.4 \pm 1.9^*$	Inferred
K_{RV} (m s^{-1}) from mass–radius relationships	$2.67 \pm 0.58^*$	Inferred
ρ_p ($\rho_\oplus$) from mass–radius relationships	$0.60^{+0.054}_{-0.091}$ *	Inferred

Values denoted with an asterisk were calculated using an estimated mass derived from the method outlined in Wolfgang, Rogers & Ford (2016), as described in Section 6.1. For T_{eq}, we assume a $A_B = 0$.

custom spectral library computed from the Castelli & Kurucz (2004) model atmospheres. We find a mean effective temperature of $T_{eff} = 4800 \pm 60$ K, surface gravity of $\log g = 4.47 \pm 0.05$ dex, and metallicity of [m/H] $= 0.0 \pm 0.05$ dex, with uncertainties adapted from the uncertainty floor as per Brahm et al. (2017). We do not incorporate the HARPS observations towards our spectroscopic parameters due to the sample being too small. We instead adopt the CHIRON and MINERVA-Australis spectra for our spectroscopic parameters, as we were able to test the self consistency of our parameters via its scatter from spectrum to spectrum (as presented in Table 3).

In addition, as the HARPS spectra cover the Calcium H&K lines, we also make use of the two available spectra to compute activity indices for HIP 113103. We followed the same procedure as per the Mt Wilson catalogue (Vaughan, Preston & Wilson 1978; Wilson 1978; Duncan et al. 1991; Baliunas et al. 1995), and compute the S-index via a set of photometric band passes about the line cores and continuum around each line. The S-index is then converted to the $\log R'_{HK}$ index as per Noyes et al. (1984). We found a mean Calcium H K activity of $\log R'_{HK} = -4.69 \pm 0.05$ from the two HARPS observations, indicating minimal chromospheric activity being exhibited by the host star (Henry et al. 1996).
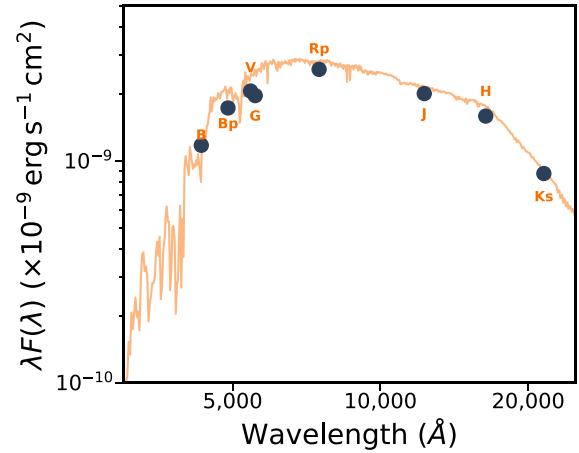
3 GLOBAL MODEL

In order to constrain the stellar and planetary properties of the HIP 113 103 system, we performed a global model fit using all the observations outlined in Section 2. Our global model is similar to that implemented in previous papers (e.g. Zhou et al. 2022), and was tested against other publicly available codes such as EXOFASTV2 in Rodriguez et al. (2017). Free parameters fitted for include orbital parameters defining the orbital eccentricity $\sqrt{e}\cos\omega$ and $\sqrt{e}\sin\omega$ (where e is eccentricity and ω is argument of periapsis), line-of-sight inclination i, orbital period P, radius ratio $R_\mathrm{p}/R_\star$, and transit midpoint T_0. The photometric transits are modeled via BATMAN (Kreidberg 2015) as per Mandel & Agol (2002), simultaneously incorporating an associated instrument model to account for additional variability induced by external factors. This includes fitting for a polynomial accounting for the influence of spacecraft on the photometric fluxes for *CHEOPS* as per Maxted et al. (2022), described in Section 2.2. Similarly, we also fit for linear coefficients to the mean, standard deviation, and skew terms of the three quarternions for *TESS* as per Vanderburg et al. (2019). Ground based LCO photometry were simultaneously detrended against airmass to remove hours time-scale variability in the baseline. Limb darkening coefficients are interpolated from the CHIRON stellar atmospheric parameters for the host star via Claret & Bloemen (2011) and Claret (2017), and constrained by Gaussian priors with widths of 0.02. The width of the Gaussian prior is set by the uncertainties in the models, and by the propagated uncertainties from the spectroscopically derived stellar parameters. We also trialled the same global model, but with Gaussian priors of width 0.1 for the limb darkening parameters and note no significant changes to our model posteriors. Supersampling corrections of the light curve model has been applied where necessary when modelling the 30-min cadenced observations (Kipping 2010). The CHIRON and MINERVA-Australis radial velocities were modeled via the RADVEL package (Fulton et al. 2018), accounting for their respective instrumental offsets and velocity jitter terms.

To jointly model the stellar properties, we interpolate the MIST isochrones (Dotter 2016) along age, stellar mass, and metallicity, with outputs of stellar radius and absolute magnitudes in a set of photometric bands as is made available by the public isochrone files. The spectral energy distribution and *Gaia* parallax provide the tightest observational constraints on the host star properties. At each iteration, we include jump parameters for age, host star mass $M_\star$, metallicity [M/H], and parallax. The parallax of the target is strongly constrained by a Gaussian prior about that measured by *Gaia* DR3 (Gaia Collaboration 2022), with a correction of -0.025657 mas applied according to Lindegren et al. (2021). We compare the interpolated MIST absolute magnitudes against that of the observed *Hipparcos* TYCHO B, and V, 2MASS J, H, and K, and the *Gaia G*, B_p, and R_p bands (Perryman et al. 1997; Skrutskie et al. 2006; Gaia Collaboration 2018) magnitudes, after correcting for the distance modulus via the parallax jump parameter. In addition to the absolute magnitudes, we also interpolate the MIST isochrones along stellar radius, which is then incorporated into modelling of the transit parameters, such as $a/R_\star$.

We constrained our models using a Markov chain Monte Carlo analysis via EMCEE (Foreman-Mackey et al. 2013), with 400 walkers over 4000 iterations per walker (with the first 2000 iterations allocated to burn in). Informative priors are summarised in Table 4, while all other fitted parameters are constrained by uniform priors bounded by their physical limits. The derived planetary and stellar values are presented in Tables 4 and 3, respectively. Fig. 1 shows our output model for our *TESS* data set, Fig. 5 for *CHEOPS*, and Fig. 6 for ground based photometric follow-up observations.
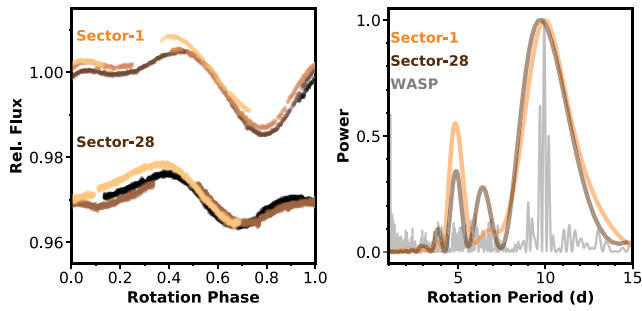
Figure 7. Spectral energy distribution of HIP 113103. We make use of the spectroscopic atmospheric priors and the photometric magnitudes of HIP 113103 to constrain the stellar properties simultaneously to our global modeling of the stellar and planetary parameters.

4 STELLAR ROTATION AND AGE

The *TESS* light curve of HIP 113103 exhibits significant quasi-periodic variability at the 0.5 per cent level representative of rotational variability. Fig. 7 shows the auto-correlation function of the periodicity over the two *TESS* sectors. We found a rotation period of 10.2 ± 1.4 d from Sector 1, and 10.0 ± 1.3 d from Sector 28 observations. The uncertainties were estimated by taking the width of the best-fitting Gaussian to the periodogram peaks. The rotation period is consistent between the two sectors, spanning 1 yr in separation.

In addition, HIP 113103 also received 1 yr of observations from the Wide Angle Search for Planets (WASP) Consortium (Pollacco et al. 2006) with the Southern SuperWASP facility, located at the Sutherland Station of the SAAO. The SuperWASP observatory consists of eight Canon 200-mm f/1.8 telephoto lenses, yielding a $7.8° \times 7.8°$ field of view each over a 2K × 2K detector. Super-WASP observations of HIP 113103 spanned 2006-05-07 to 2007-11-13, yielding ~11 000 epochs of observations. The periodogram from the SuperWASP light curves are also overplotted in Fig. 8, yielding a rotation period of 9.90 ± 0.23 d, consistent with the *TESS* observations more than a decade later. When combined, the *TESS* and WASP data sets provide a long term stable rotation period of 9.92 ± 0.23 d for HIP 113103. In addition, we make use of the measured rotational velocity $v\sin I_\star$ and the photometric rotation period to provide a 1σ lower limit for the stellar inclination angle of $I_\star > 56°$ (Masuda & Winn 2020), consistent with an aligned geometry. Using $R_\star = 0.742 \pm 0.013\,R_\odot$ and $P_\mathrm{rot} = 9.92 \pm 0.23$ d, we also calculate an equatorial velocity of $V_\mathrm{eq} = 3.78 \pm 0.11\,\mathrm{km\,s^{-1}}$, which is in good agreement with our $v\sin i$ value of $3 \pm 1\,\mathrm{km\,s^{-1}}$.

The rotation period of HIP 113103 is consistent with an adolescent K dwarf. We adopt the rotation sequence interpolation presented by Bouma et al. (2023), and derive a rotation-based age of 470^{+170}_{-110} Myr at 1σ significance. Similarly, based on the rotation age relationship from Mamajek & Hillenbrand (2008), the 1σ age range for HIP 113103 is 380–510 Myr. However, gyrochronology is particularly insecure in estimating the ages of single K dwarfs. The spins of these stars may stall within the first billion years, and many around giga-year clusters exhibit similar rotation periods (e.g. Meibom, Mathieu & Stassun 2009; Agüeros et al. 2018; Douglas et al. 2019). Angus et al. (2015) accounts for a larger spread in the spin-down

Figure 8. Spectral energy distribution of HIP 113103. We make use of the spectroscopic atmospheric priors and the photometric magnitudes of HIP 113103 to constrain the stellar properties simultaneous to our global modeling of the stellar and planetary parameters. HIP 113103 exhibits significant spot-induced rotational variability in its light curves. Left: *TESS* light curves from Sectors 1 and 28 folded to the rotation period of HIP 113103; each rotation cycle is plotted in a progressively lighter shade. The sectors are separated by an arbitrary vertical offset. HIP 113103 maintains a constant rotation period over the multiyear observations obtained by *TESS*. Right: Autocorrelation periodograms of the *TESS* and SuperWASP light curves of HIP 113103, showing a consistent peak at 10.0 d over the course of more than 10 yr.

dispersion of low mass stars, and the relationship they provide yields a 1σ age range of 200–2000 Myr for HIP 113103. HIP 113103 lacks spectroscopic features, such as Li 6708 Å absorption and significant Calcium II H&K emission that are usually indicative of youth, as is expected for K dwarfs older than $\sim$300 million yr (Fig. 7). The Calcium II H&K derived index log $R'_{\rm HK} = -4.69 \pm 0.05$ corresponds to an age of $1.9^{+0.7}_{-0.5}$ Gyr, consistent with the rotational derived age estimate. In addition, the isochrone modelling also provides a loose age constraint of 5 ± 2 Gyr at the 1σ level. We find no evidence that HIP 113103 is kinematically associated with comoving stars via the COMOVE package (Tofflemire et al. 2021).[2] It is therefore difficult to confirm the suspected youth of HIP 113103.

5 INVESTIGATING FALSE POSITIVE SCENARIOS

When identifying a new planetary system, it is important to carefully consider the possibilities of astrophysical and instrumental false positives.

When analysing beyond the *TESS* observations, HIP 113103 b and HIP 113103 c are detected with high significance on multiple instruments, yielding consistent transit depth and duration and thus sufficiently ruling out the scenario that the transit signals result from instrument false alarms of the *TESS* spacecraft.

We use the following steps to rule out various astrophysical false positive scenarios. We can determine that either HIP 113103 b or HIP 113103 c are not eclipsing binaries around HIP 113103 using radial velocity observations taken with CHIRON as outlined in Section 2.4. There were no detections of significant radial velocity variations at the 20 m s^{-1} level, ruling out stellar mass objects at the orbital period of the transit signals.

We then follow Seager & Mallén-Ornelas (2003) to use the transit shapes to constrain the probability that the transit signals were mimicked by a binary system blended with the HIP 113103. The maximum magnitude of an eclipsing binary that can produce a transit

[2]https://github.com/adamkraus/Comove

with similar shape can be estimated by

$$\Delta M \lesssim 2.5 \log_{10} \left(\frac{t_{12}^2}{t_{13}^2 \delta} \right)^2, \tag{1}$$

where t_{12} represents the ingress duration, and t_{13} represent the time between the first and the third contact of the transit.

We model the transit shape of both planets independently using the *TESS* and *CHEOPS* light curves without putting any priors on the stellar parameters. We found the 3σ $T_{\rm mag}$ upper limit of any background stars capable of producing these transit signals are 13 ($\Delta M < 4.23$ mag) and 12 ($\Delta M < 3.06$ mag) for HIP 113103 b and HIP 113103 c, respectively.

We rule out an hierarchical binary system associated with HIP 113103, satisfying the above criteria. Neither CHIRON nor the HARPS observations (Section 2.4) detected secondary spectra lines, indicating no slow rotating, spectroscopic blended companions at $\Delta M < 4$ (Zhou et al. 2021).

For non-associated background binaries, we can use the *Gaia* DR3 catalogue to rule out stars brighter than our magnitude limit up to 1 arcmin away from HIP 113103. There are no stars within 20 arcsec of HIP 113 103 based on Gaia DR3 catalogue. We estimate the density of stars brighter than our magnitude limit within 1 arcmin of HIP 113103 (which may be unresolved) by following the procedure described in Zhou et al. (2021). We found that the chance of finding a random star in the direction of HIP 113103 with $\Delta M < 4.2$ and $\Delta M < 3$ are 3×10^{-5} and 1×10^{-5}.

Taken together, the combined observations that the system hosts multiple planets, the box-shaped transits, and the lack of additional stars in the spectra and background give us high confidence that HIP 113103 b and HIP 113103 c are genuine planets.

We also conducted a statistical validation on the *TESS* observations using the TRICERATOPS package (Giacalone et al. 2021), the false positive probability (FPP) yielded 0.052 for HIP 113103 b and 0.026 for HIP 113103 c. The Nearby Star FPP (NFPP) for both planets is 0. The main contributor to the FPP is the scenario that a transiting planet with the same period is around an unresolved secondary star (known as STP). We have high confidence that CHIRON and HARPS spectra can rule out secondary stars in the same system within Δmag of 4, which is the magnitude limit to cause a transit given the transit shape constraints. The rest of false positive scenario have total FPP less than 1e-3, therefore we can confidently call both candidates planets.

6 RESULTS AND DISCUSSION

6.1 Planet properties

We statistically validate the planetary nature of the HIP 113103 system, with the best-fitting planetary parameters presented in Table 4. HIP 113103 b has a radius of $R_{\rm p} = 1.829^{+0.096}_{-0.067}$ R$_\oplus$, placing it in the upper bound of the radius gap, a small population of planets within the radii bounds 1.5 R$_\oplus < R_{\rm p} \leq 2$ R$_\oplus$ which may be the transition point from super-Earths to mini-Neptunes via photoevaporation-driven mass loss (Fulton et al. 2017). HIP 113103 c has a radius of $R_{\rm p} = 2.40^{+0.10}_{-0.08}$ R$_\oplus$, and an equilibrium temperature of 585 ± 10 K, making it a warm mini-Neptune.

We compare the HIP 113103 system with other K stars hosting multisub-Neptune planets with $T_{\rm eq} \leq 750$ K in (Fig. 9), evaluating the transmission spectroscopy metric (TSM) for each target (Kempton et al. 2018). Due to the relative brightness of HIP 113103 (V $\sim$10 mag) and high equilibrium temperatures, HIP 113103 b (TSM = 53) and HIP 113103 c (TSM = 68) are the second most suited system around a K star for atmosphere characterization [only succeeded
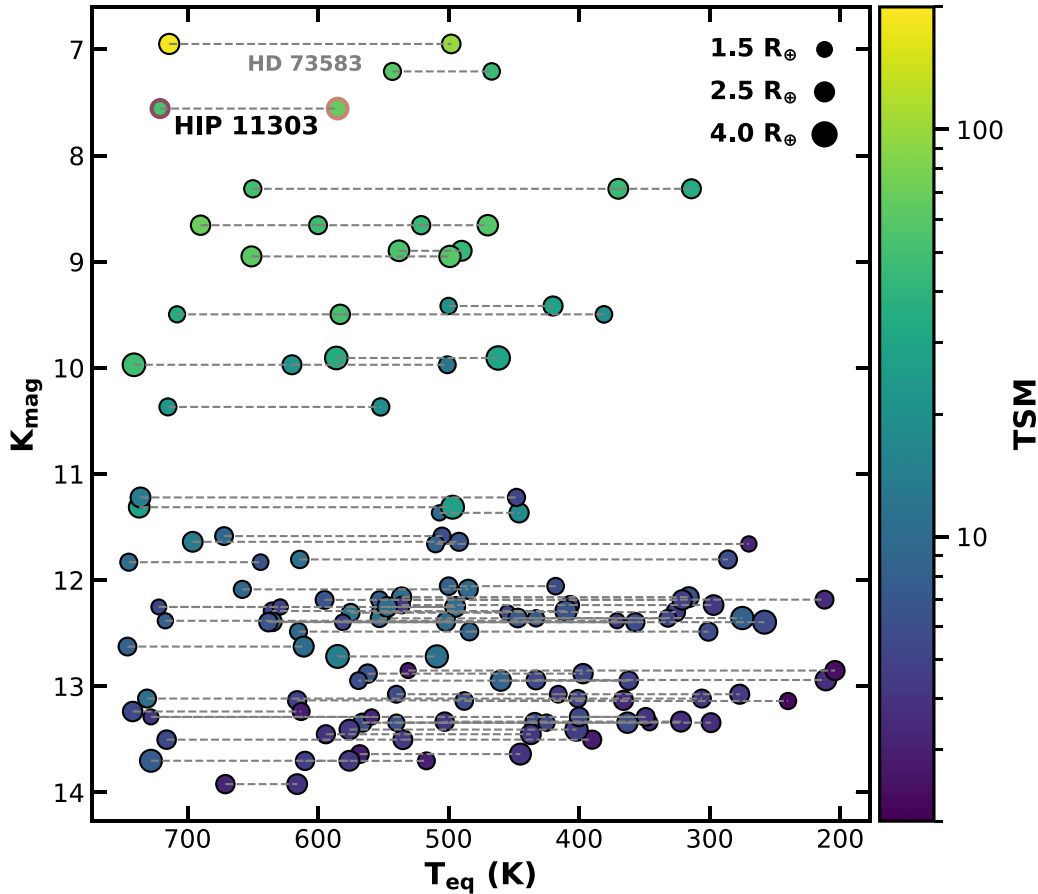
Figure 9. The HIP 113103 system in the context of other multiplanet systems. Specifically, we show multiplanet systems hosting two or more warm Neptunes or super-Earths with equilibrium temperature $T_{eq} \leq 750$ K, orbiting K stars as a function of their equilibrium temperature and K-band magnitude. The dashed lines connect each planet within the respective planetary system. The HIP 113103 system orbits one of the brightest K-dwarf host stars, and are promising candidates for follow up atmospheric observations. The colour bar illustrating the TSM for each planet places the HIP 113103 system as second highest suitable for atmosphere analysis, behind the HD 73 583 system (Barragán et al. 2022).

by the HD 73 583 system (Barragán et al. 2022)], and therefore invaluable targets to understand how multisub-Neptune systems might evolve around K-stars. This stellar population is optimal for radial velocity due to its brightness in comparison to planets orbiting M-dwarfs (Neil & Rogers 2018; Rojas-Ayala 2023). This aids the detection of smaller planets around a stellar population that shares similar characteristics to G-stars (Howard et al. 2012). Additionally from an atmosphere analysis perspective, K-stars have had repeated success at hosting planets with absorption at the He I 10 830 Å line, a tracer associated with atmosphere evaporation (Nortmann et al. 2018; Allart et al. 2019; Guilluy et al. 2020; Fu et al. 2022). Although the TSM values for HIP 113103 b and HIP 113103 c are below the J-band priority threshold of 90 (for targets within the $1.5 \, R_{\oplus} \leq R_p \leq 10 \, R_{\oplus}$), the derived radii of the planets combined with their close proximity to HIP 113103, and its Gyrochronological age make it a valuable system to explore through atmosphere analysis.

To estimate the mass of both planets to gauge the feasibility of future follow-up observations, we adopt the mass–radius relationship from Wolfgang et al. (2016). We estimate $M_p = 5.9 \pm 1.9 \, M_{\oplus}$ for HIP 113103 b and $M_p = 8.4 \pm 1.9 \, M_{\oplus}$ for HIP 113103 c. These correspond to radial velocity semi-major amplitudes of 2.34 m s^{-1} and 2.67 m s^{-1}, respectively. Additional analysis using the Echelle SPectrograph for Rocky Exoplanets and Stable Spectroscopic Ob-

servations (ESPRESSO; Pepe et al. 2021) instrument on the Very Large Telescope (VLT) to understand this system in greater detail is currently underway.

6.2 Transit timing variations

We search for transit timing variations (TTVs), indicative of interactions between the two planets, or the presence of additional companions. To derive accurate transit times for each event, we perform an additional global model of the system, as per Section 3, where the transit epoch of each transit event is a free variable, and the period is held fixed. The resulting transit times are displayed in Fig. 10. We find no evidence for deviations from a linear ephemeris propagation larger than 4.5 (resp. 2.5) min (1σ scatter) for HIP 113103 b (resp. c). The mean timing uncertainty per transit is 5.7 (resp. 3.3) min, consistent with the measured scatter. We estimated the expected TTV amplitude for the system using TTVFASTER (Agol & Deck 2016). Given the pair of planets has a period ratio within 10 per cent of the 2:1 mean motion resonance, we can estimate that if the planets are on modest eccentric orbits or are relatively massive, they are highly likely to exhibit TTVs with amplitudes detectable by our observations. In detail, if both planets are of Neptune mass ($\sim$17 M$_{\oplus}$), and we assume relatively low eccentricities follow a Rayleigh distribution
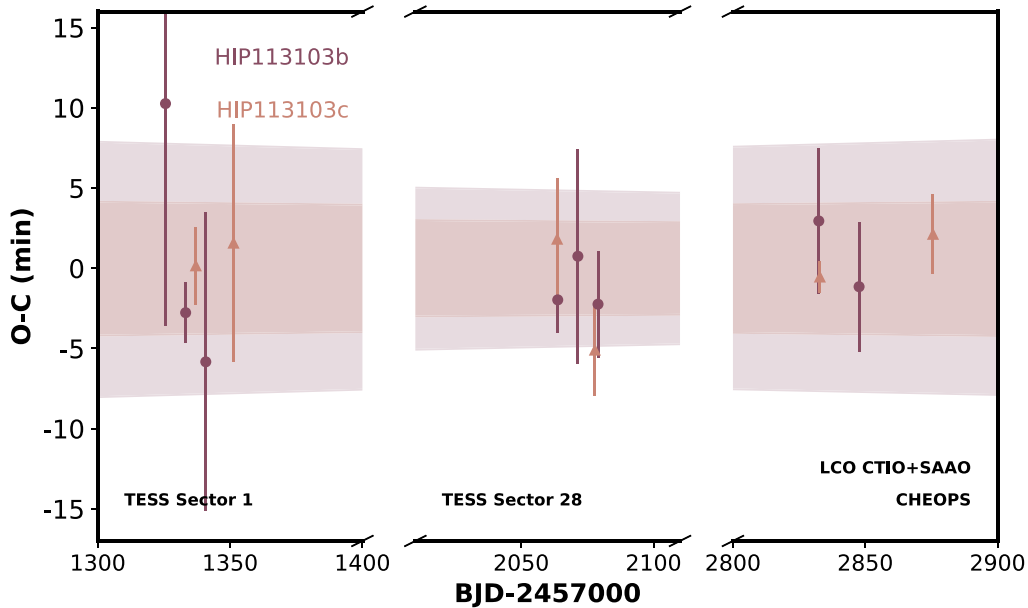
Figure 10. Deviations from linear transit times for individual transits of HIP 113103 b (circle markers) and HIP 113103 c (triangle markers) from all photometric observations, with each facility identified via labels along the time axis. Using our global fitted T_0 values to serve as the linear baseline for HIP 113103 b and HIP 113103 c, we show that over a 4-yr period, the transit midpoint for each target does not vary beyond ∼10 min shaded regions denote the 1σ propagated transit timing uncertainties for each respective planet. Note that the individual transit times are fully consistent with the linear transit ephemeris.

with $\sigma_e = 0.06$ (consequent mean eccentricity, $\bar{e} = 0.075$), the median TTV scatter for HIP 113103 b (resp. HIP 113103 c) should be on the 10 (resp. 15) min time-scale (Jurić & Tremaine 2008). If we adopt masses for both planets as per the mass–radius relationship from Wolfgang et al. (2016), TTVFASTER estimates that the eccentricity of the system is most likely lower than 0.2 given the non-detection of a significant TTV signal. This puts tighter constraints on the system eccentricity compared to our global modeling. This eccentricity upper limit is derived by comparing the scatter in the transit times from TTVFASTER simulations and the observed data. We first compute the 3 sigma scatter of the transit times from the data set presented in Fig. 10. We then compute the corresponding eccentricities of the systems that would produce larger transit time deviations in 95 per cent of the simulations.

$$95\% \tag{2}$$

6.3 Prospect for atmospheric follow-up

Systems hosting transiting small planets are optimal for understanding the radius evolution and mass-loss processes that sculpt the close-in sub-Neptune population (e.g. Owen & Campos Estrada 2020). Having planets that formed from the same protoplanetary disc and experienced the same host star XUV evolution, allows us to test photoevaporation processes by isolating the effects of insulation on mass-loss. We tested for the future prospect of atmospheric transmission spectroscopic observations for the planets in the HIP 113103 system via a set of current and upcoming space-based facilities, including the *Twinkle Space Telescope* (*Twinkle*; Stotesbury et al. 2022), *HST* (Kimble et al. 2008; Tsiaras et al. 2016), and *JWST* (Bean et al. 2018; Jakobsen et al. 2022). *Twinkle* is a visible to infrared (0.5 μm−4.5 μm) 0.45-m space telescope set to begin scientific operations in 2025 at a 700 km geocentric Sun-synchronous orbit.

The simulated transmission *Twinkle* spectra is generated for both channels (0.5 μm ≤ Ch0 ≤ 2.43 μm, 2.43 μm ≤ Ch1 ≤

4.5 μm) using the radiometric tool available on the mission's data base Stardrive[3], while the *HST* (WFC3 NIR G141 grism: 1.075 μm−1.7 μm) and *JWST* (NIRSpec G395H grism: 2.87 μm −5.14 μm) transmission spectra are generated using the publicly available noise simulator, PANDEXO (Batalha et al. 2017). The synthetic transmission spectra are processed through the retrieval framework TAUREX 3.0 (Al-Refaie et al. 2021), which generates an atmosphere divided into 100 evenly spaced layers across a log grid varying from 10^{-4} to 10^6 Pa. The trace gases in our models were assumed to be in chemical equilibrium and the abundances were calculated using FASTCHEM (Stock et al. 2018). We keep the C/O ratio fixed at 0.54 (an oxygen rich atmosphere at solar abundances as discussed in Madhusudhan 2012) and assume a metallicity of 100 × Solar for HIP 113103 b and 10 × Solar for HIP 113103 c, aligning with previous studies that relate metallicity and low-mass planets as being inversely proportional (e.g. Fortney et al. 2013; Kreidberg et al. 2014; Charnay, Meadows & Leconte 2015). The trace gases inserted into this atmosphere included the molecular opacities of CH_4 (Hill, Yurchenko & Tennyson 2013; Yurchenko & Tennyson 2014), CO (Li et al. 2015), CO_2 (Rothman et al. 2010), H_2O (Polyansky et al. 2018), and NH_3 (Yurchenko, Barber & Tennyson 2011), with all opacities being obtained through the ExoMol (Tennyson et al. 2016) and HITRAN data bases (Gordon et al. 2016). In addition, we also implement Rayleigh scattering for all inserted molecules (Cox 2015), provide a collision induced absorption from H_2–H_2 (Abel et al. 2011; Fletcher, Gustafsson & Orton 2018) and H_2–He interactions (Abel et al. 2012). For each instrument, we modelled both a clear atmosphere scenario (i.e. $P = 10^6$ Pa) and a uniform opaque deck scenario (i.e. grey clouds) at $P = 10^1$ Pa.

We present our simulated spectra of HIP 113103 b in Fig. 11 and HIP 113103 c in Fig. 12. Should HIP 113103 b and HIP 113103 c reflect a similar composition as our simulated spectra, we can recover

---

[3]Stardrive Database
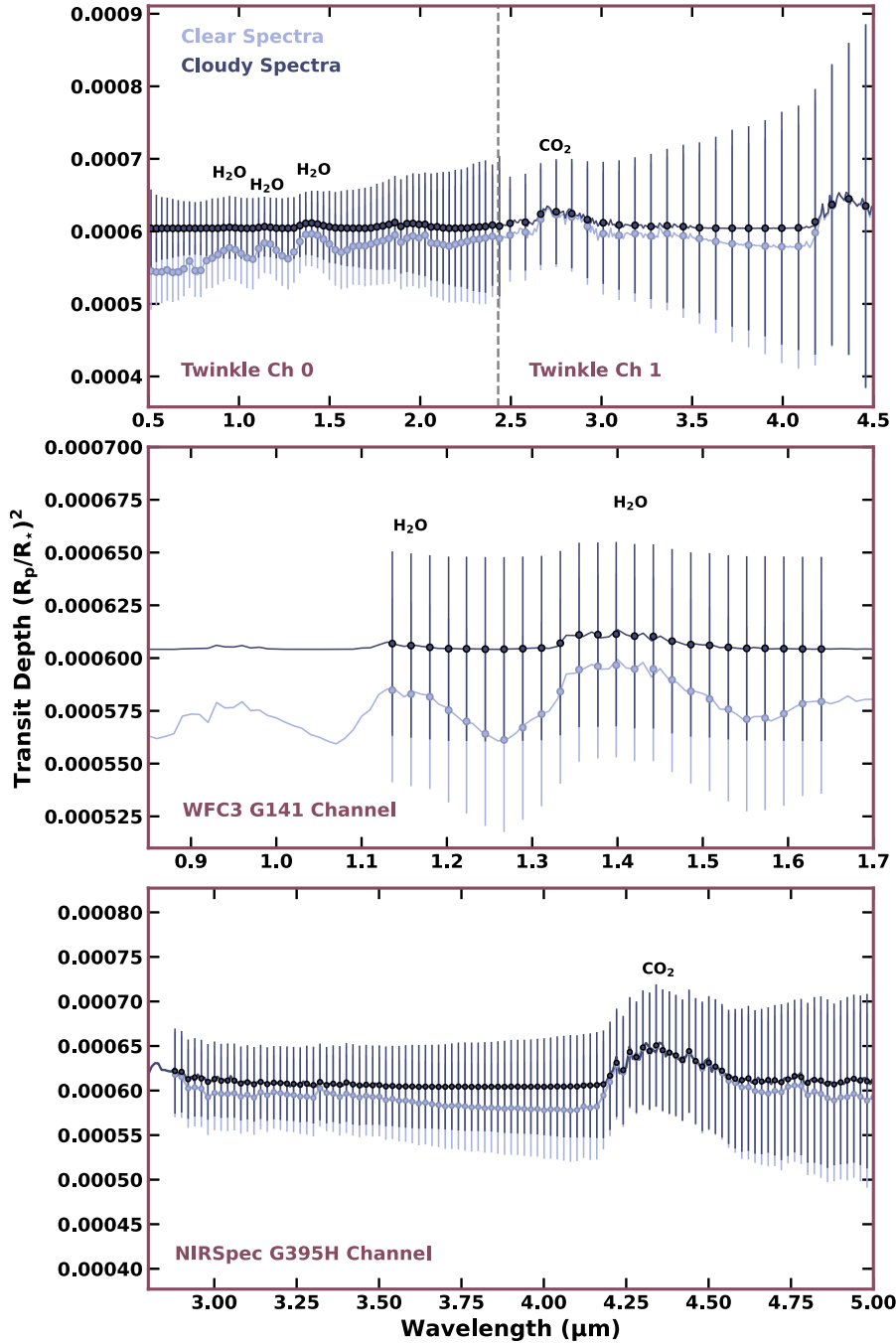
Figure 11. A synthetic atmospheric transmission spectra of HIP 113103 b, incorporating absorbing species CH_4, CO, CO_2, H_2O, and NH_3 at chemical equilibrium assuming an atmospheric metallicity of $100\times$ Solar. The top panel illustrates the expected spectrum after 10 visits with *Twinkle*, the middle panel shows the simulated spectrum from a single visit with *HST* WFC3 with the G141 grism, and the bottom panel shows the simulated spectrum from a single visit with *JWST* NIRSpec G395H grism (with each instrument capturing a different wavelength range). For each facility, we have illustrated two scenarios: one where spectrum is cloud-free (10^6 Pa), and another with a grey cloud deck (10^1 Pa). The synthetic spectra for *Twinkle* was obtained using the radiometric tool on the *Twinkle* Stardrive portal, while the *HST* and *JWST* spectra were generated using PANDEXO.

a transmission spectra from 10 orbits using *Twinkle* (top panels; Stotesbury et al. 2022). Likewise, Figs 11 and 12 demonstrate the precision we can expect to achieve from one orbit observation using the infrared WFC3 G141 grism (middle panels) on *HST* (Kimble et al. 2008; Tsiaras et al. 2016) and NIRSpec G395H grism (bottom panels) on *JWST* (Bean et al. 2018; Jakobsen et al. 2022). We can successfully retrieve molecular species for HIP 113103 c with each

instrument given a clear atmosphere (with H_2O and CO_2 displaying the strongest absorption). However, in the event of clouds, we would struggle to detect any signal for HIP 113103 c using *Twinkle* and *HST* instruments. Distinguishing between a clear or cloudy atmosphere on all three instruments is challenging for HIP 113103 b. An atmosphere that is in chemical disequilibrium for both targets could result in stronger absorption but would be dependent on various unknown
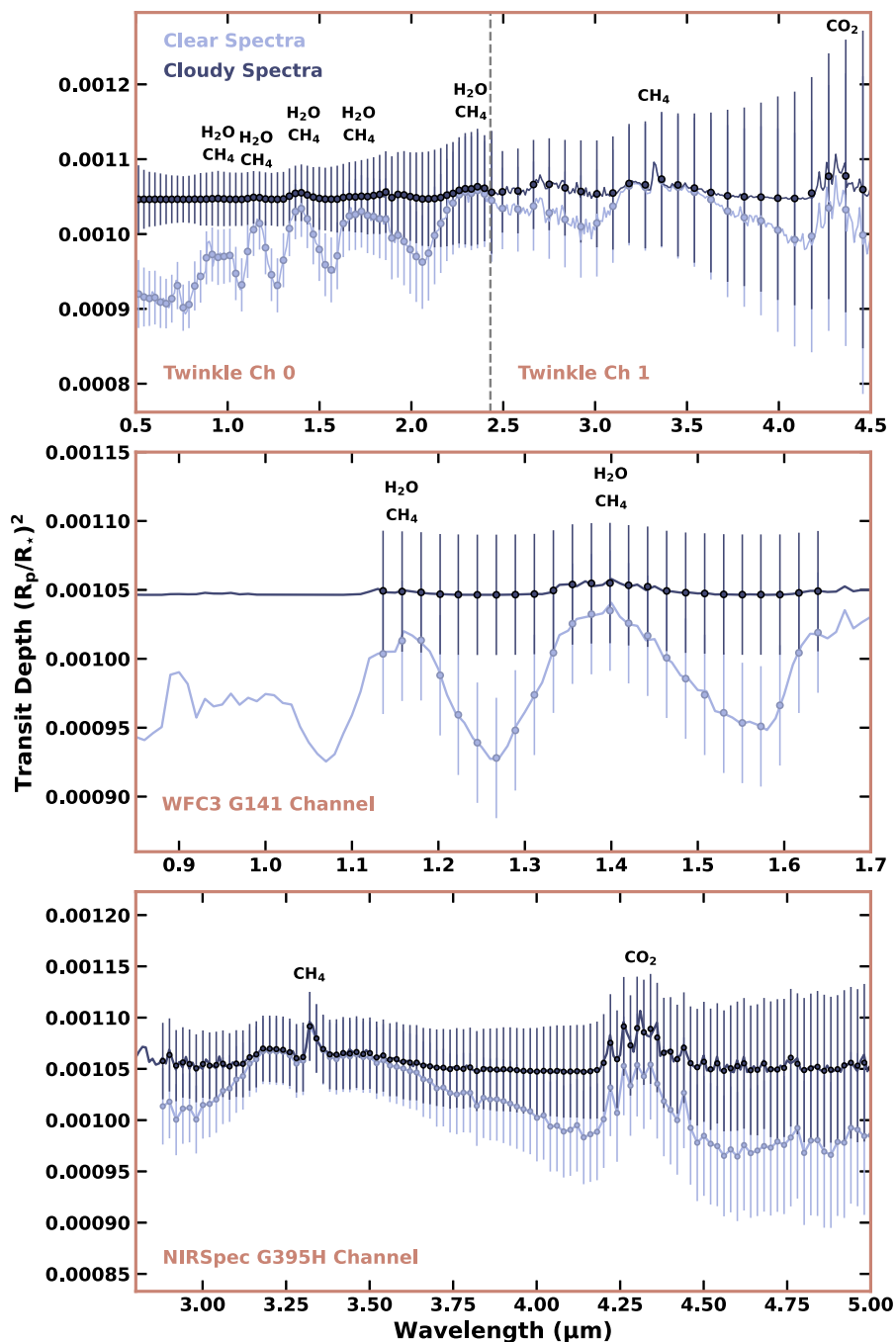
Figure 12. A synthetic atmospheric transmission spectrum of HIP 113103 c, with absorbing species including CH_4, CO, CO_2, H_2O, and NH_3 in chemical equilibrium at an atmospheric metallicity of 10×Solar. Figure configuration is as per Fig. 11, with the *Twinkle* retrieval representing 10 visits.

physical parameters. Alternatively, the evolutionary path of HIP 113103 b could be the product of a migrated Water World instead of photoevaporation of a mini-Neptune (e.g. Luque & Pallé 2022); however, this scenario can only be explored in more detail after planet density measurements have been calculated. Our density estimation for HIP 113103 b of $0.96^{+0.15}_{-0.22} \rho_\oplus$ is indicative of a rocky planet, but is inferred from a mass–radius relationship and may not reflect the true bulk density of the planet. Accurate mass measurements of HIP 113103 b and HIP 113103 c are required to confirm their densities.

7 CONCLUSION

In this paper, we confirm the existence of two sub-Neptunes, HIP 113103 b and HIP 113103 c, within $\sim 10\%$ of 2:1 resonance around the bright K3V star HIP 113103. First identified with *TESS*, this system is revisited using both ground based transit observations (observed with the photometric LCO network and on the CHIRON spectrograph), as well as a space-based photometric observations of both targets within a $\sim$17.5-h visit using *CHEOPS*. Follow up TTV analysis does not reveal any additional outer companions. Our planetary parameters revealed a radius of $R_{\rm p} = 1.829^{+0.096}_{-0.067}$ R$_\oplus$

for HIP 113103 b and $R_{\rm p} = 2.40^{+0.10}_{-0.08}$ R$_\oplus$ for HIP 113103 c, confirming both targets reside within the mini-Neptune sub-class. For HIP 113103 b, the combination of its close proximity to HIP 113103 and its planetary radius means it resides within the radius gap, which if confirmed via mass follow up, would add an additional target a sparse sub-class of planets which are hypothesized to bridge the formation transition between super-Earths and mini-Neptunes. If HIP 113103 b is the subject of atmosphere evaporation due to its close proximity to HIP 113103, our generated retrieval plots (using the *Twinkle*, *HST*, and *JWST* telescopes) suggest it would be a struggle to distinguish an evolutionary gap via metallicity disparity for all three telescopes (assuming chemical equilibrium), even if there is a clear atmosphere. Ultimately, this system provides two key targets capable of atmospheric analysis within the population of mini-Neptune multiplanet systems orbiting K-stars.

ACKNOWLEDGEMENTS

DATA AVAILABILITY

The data underlying this article will be shared on reasonable request to the corresponding author.

REFERENCES

Abel M., Frommhold L., Li X., Hunt K. L., 2011, J. Phys. Chem. A, 115, 6805
Abel M., Frommhold L., Li X., Hunt K. L., 2012, J. Chem. Phys., 136, 44319
Addison B. et al., 2019, PASP, 131, 115003
Agol E., Deck K., 2016, ApJ, 818, 177
Agüeros M. A. et al., 2018, ApJ, 862, 33
Ahrer E.-M. et al., 2023, Nature, 614, 653
Al-Refaie A. F., Changeat Q., Waldmann I. P., Tinetti G., 2021, ApJ, 917, 37
Alderson L. et al., 2023, Nature, 614, 664
Allart R. et al., 2019, A&A, 623, A58
Angus R., Aigrain S., Foreman-Mackey D., McQuillan A., 2015, MNRAS, 450, 1787
Baliunas S. L. et al., 1995, ApJ, 438, 269
Barnes S. I., Gibson S., Nield K., Cochrane D., 2012, in McLean I. S., Ramsay S. K., Takami H.eds, SPIE Conf. Ser. Vol. 8446, Ground-based and Airborne Instrumentation for Astronomy IV. SPIE, Bellingham. p. 844688
Barragán O. et al., 2022, MNRAS, 514, 1606
Batalha N. E. et al., 2017, PASP, 129, 64501
Bean J. L. et al., 2018, PASP, 130, 114402
Bean J. L., Raymond S. N., Owen J. E., 2021, J. Geophys. Res. (Planets), 126, e06639
Benneke B. et al., 2019, Nature Astron., 3, 813
Benz W. et al., 2021, Exp. Astron., 51, 109
Bergsten G. J., Pascucci I., Mulders G. D., Fernandes R. B., Koskinen T. T., 2022, AJ, 164, 5
Bouma L. G., Palumbo E. K., Hillenbrand L. A., 2023, ApJ, 947, L3
Brahm R., Jordán A., Hartman J., Bakos G., 2017, MNRAS, 467, 971
Brandt T. D., 2021, ApJS, 254, 42
Brown T. M. et al., 2013, PASP, 125, 1031
Buchhave L. A. et al., 2012, Nature, 486, 375
Castelli F., Kurucz R. L., 2004, preprint (arXiv:Astrophysics e-prints)
Charnay B., Meadows V., Leconte J., 2015, ApJ, 813, 15
Claret A., 2017, A&A, 600, A30
Claret A., Bloemen S., 2011, A&A, 529, A75
Cloutier R. et al., 2020, AJ, 160, 3
Collins K. A., Kielkopf J. F., Stassun K. G., Hessman F. V., 2017, AJ, 153, 77

Cox A. N., 2015, in Allen's Astrophysical Quantities. Springer, United Kingdom, p. 721

Cutri R. M. et al., 2012, VizieR Online Data Catalog, p. II/311

Czesla S., Schröter S., Schneider C. P., Huber K. F., Pfeifer F., Andreasen D. T., Zechmeister M., 2019, PyA: Python astronomy-related packages, preprint (ascl:1906.010)

Delrez L. et al., 2021, Nature Astron., 5, 775

Donati J.-F., Semel M., Carter B. D., Rees D. E., Collier Cameron A., 1997, MNRAS, 291, 658

Dotter A., 2016, ApJS, 222, 8

Douglas S. T., Curtis J. L., Agüeros M. A., Cargile P. A., Brewer J. M., Meibom S., Jansen T., 2019, ApJ, 879, 100

Dragomir D. et al., 2019, ApJ, 875, L7

Duncan D. K. et al., 1991, ApJS, 76, 383

Edwards B. et al., 2022, preprint (arXiv:2211.00649)

Feinstein A. D. et al., 2023, Nature, 614, 670

Fletcher L. N., Gustafsson M., Orton G. S., 2018, ApJS, 235, 24

Foreman-Mackey D., Hogg D. W., Lang D., Goodman J., 2013, PASP, 125, 306

Fortney J. J., Mordasini C., Nettelmann N., Kempton E. M. R., Greene T. P., Zahnle K., 2013, ApJ, 775, 80

Fressin F. et al., 2013, ApJ, 766, 81

Fu G. et al., 2022, ApJ, 940, L35

Fulton B. J. et al., 2017, AJ, 154, 109

Fulton B. J., Petigura E. A., Blunt S., Sinukoff E., 2018, PASP, 130, 44504

Gaia Collaboration, 2018, A&A, 616, A1

Gaia Collaboration, 2022, A&A, 674, A1

Gan T. et al., 2022, MNRAS, 514, 4120

Gandolfi D. et al., 2018, A&A, 619, L10

Gandolfi D. et al., 2019, ApJ, 876, L24

Giacalone S. et al., 2021, AJ, 161, 24

Ginzburg S., Schlichting H. E., Sari R., 2018, MNRAS, 476, 759

Gordon I., Rothman L. S., Wilzewski J. S., Kochanov R. V., Hill C., Tan Y., Wcislo P., 2016, in AAS/Division for Planetary Sciences Meeting Abstracts #48. p. 421.13

Gray R. O., Corbally C. J., 1994, AJ, 107, 742

Greene T. P., Line M. R., Montero C., Fortney J. J., Lustig-Yaeger J., Luther K., 2016, ApJ, 817, 17

Guerrero N. M. et al., 2021, ApJS, 254, 39

Guilluy G. et al., 2020, A&A, 639, A49

Henry T. J., Soderblom D. R., Donahue R. A., Baliunas S. L., 1996, AJ, 111, 439

Hill C., Yurchenko S. N., Tennyson J., 2013, Icarus, 226, 1673

Høg E. et al., 2000, A&A, 355, L27

Howard A. W. et al., 2012, ApJS, 201, 15

Howe A. R., Burrows A., 2015, ApJ, 808, 150

Huang C. X. et al., 2020a, Res. Notes Am. Astron. Soc., 4, 204

Huang C. X. et al., 2020b, Res. Notes Am. Astron. Soc., 4, 206

Huang X., Bakos G. Á., Hartman J. D., 2013, MNRAS, 429, 2001

Jakobsen P. et al., 2022, A&A, 661, A80

Jenkins J. M. et al., 2016, in Software and Cyberinfrastructure for Astronomy IV. p. 99133E

Jurić M., Tremaine S., 2008, ApJ, 686, 603

Kawauchi K. et al., 2022, A&A, 666, A4

Kempton E. M. R. et al., 2018, PASP, 130, 114401

Ketzer L., Poppenhaeger K., 2022, MNRAS, 518, 1683

Kimble R. A., MacKenty J. W., O'Connell R. W., Townsend J. A., 2008, in Oschmann Jacobus M. J., de Graauw M. W. M., MacEwen H. A.eds, SPIE Conf. Ser. Vol. 7010, Space Telescopes and Instrumentation 2008: Optical, Infrared, and Millimeter. SPIE, Bellingham. p. 70101E

Kipping D. M., 2010, MNRAS, 408, 1758

Kite E. S., Barnett M. N., 2020, Proc. Natl. Acad. Sci., 117, 18264

Kite E. S., Fegley Bruce J., Schaefer L., Ford E. B., 2020, ApJ, 891, 111

Kovács G., Zucker S., Mazeh T., 2002, A&A, 391, 369

Kreidberg L. et al., 2014, Nature, 505, 69

Kreidberg L., 2015, PASP, 127, 1161

Li G., Gordon I. E., Rothman L. S., Tan Y., Hu S.-M., Kassi S., Campargue A., Medvedev E. S., 2015, ApJS, 216, 15

Lindgren L. et al., 2021, A&A, 649, A4

Lopez E. D., Fortney J. J., Miller N., 2012, ApJ, 761, 59

Lubin J. et al., 2022, AJ, 163, 101

Luque R., Pallé E., 2022, Science, 377, 1211

MacDougall M. G. et al., 2021, AJ, 162, 265

Madhusudhan N., 2012, ApJ, 758, 36

Mamajek E. E., Hillenbrand L. A., 2008, ApJ, 687, 1264

Mandel K., Agol E., 2002, ApJ, 580, L171

Masuda K., Winn J. N., 2020, AJ, 159, 81

Maxted P. F. L. et al., 2022, MNRAS, 514, 77

Mayor M. et al., 2003, Messenger, 114, 20

Mazeh T., Faigler S., 2010, A&A, 521, L59

McCully C., Volgenau N. H., Harbeck D.-R., Lister T. A., Saunders E. S., Turner M. L., Siiverd R. J., Bowman M., 2018, in Proc. SPIE. 10707, p.107070K

Meibom S., Mathieu R. D., Stassun K. G., 2009, ApJ, 695, 679

Mordasini C., 2020, A&A, 638, A52

Morris R. L., Twicken J. D., Smith J. C., Clarke B. D., Jenkins J. M., Bryson S. T., Girouard F., Klaus T. C., 2020, Kepler Data Processing Handbook: KSCI-19081-003

Mugnai L. V. et al., 2021, AJ, 161, 284

Neil A. R., Rogers L. A., 2018, ApJ, 858, 58

Nortmann L. et al., 2018, Science, 362, 1388

Noyes R. W., Hartmann L. W., Baliunas S. L., Duncan D. K., Vaughan A. H., 1984, ApJ, 279, 763

Orell-Miquel J. et al., 2022, A&A, 659, A55

Osborn A. et al., 2021, MNRAS, 507, 2782

Owen J. E., Campos Estrada B., 2020, MNRAS, 491, 5287

Owen J. E., Jackson A. P., 2012, MNRAS, 425, 2931

Paredes L. A., Henry T. J., Quinn S. N., Gies D. R., Hinojosa-Goñi R., James H.-S., Jao W.-C., White R. J., 2021, AJ, 162, 176

Pepe F. et al., 2021, A&A, 645, A96

Perryman M. A. C. et al., 1997, A&A, 323, L49

Pollacco D. L. et al., 2006, PASP, 118, 1407

Polyansky O. L., Kyuberis A. A., Zobov N. F., Tennyson J., Yurchenko S. N., Lodi L., 2018, MNRAS, 480, 2597

Ricker G. R. et al., 2015, J. Astron. Telescopes Instrum. Syst., 1, 14003

Rodriguez J. E. et al., 2017, AJ, 153, 256

Rodriguez J. E., Vanderburg A., Eastman J. D., Mann A. W., Crossfield I. J. M., Ciardi D. R., Latham D. W., Quinn S. N., 2018, AJ, 155, 72

Rojas-Ayala B., 2023, preprint (arXiv:2301.03442)

Rothman L. et al., 2010, J. Quant. Spectrosc. Radiat. Transfer, 111, 2139

Rustamkulov Z. et al., 2023, Nature, 614, 659

Scarsdale N. et al., 2021, AJ, 162, 215

Seager S., Mallén-Ornelas G., 2003, ApJ, 585, 1038

Skrutskie M. F. et al., 2006, AJ, 131, 1163

Sozzetti A. et al., 2021, A&A, 648, A75

Stassun K. G. et al., 2019, AJ, 158, 138

Stock J. W., Kitzmann D., Patzer A. B. C., Sedlmayr E., 2018, MNRAS, 479, 865

Stotesbury I. et al., 2022, in Coyle L. E., Matsuura S., Perrin M. D.eds, SPIE Conf. Ser. Vol. 12180, Space Telescopes and Instrumentation 2022: Optical, Infrared, and Millimeter Wave. SPIE, Bellingham. p. 1218033.

Tennyson J. et al., 2016, J. Mol. Spectrosc., 327, 73

Teske J. et al., 2020, AJ, 160, 96

Tinetti G. et al., 2018, Exp. Astron., 46, 135

Tofflemire B. M. et al., 2021, AJ, 161, 171

Tokovinin A., Fischer D. A., Bonati M., Giguere M. J., Moore P., Schwab C., Spronck J. F. P., Szymkowiak A., 2013, PASP, 125, 1336

Tsai S.-M. et al., 2023, Nature, 617, 483

Tsiaras A. et al., 2016, ApJ, 820, 99

Tsiaras A., Waldmann I. P., Tinetti G., Tennyson J., Yurchenko S. N., 2019, Nature Astron., 3, 1086

Twicken J. D., Clarke B. D., Bryson S. T., Tenenbaum P., Wu H., Jenkins J. M., Girouard F., Klaus T. C., 2010, in Software and Cyberinfrastructure for Astronomy. p. 774023

Vanderburg A. et al., 2019, ApJ, 881, L19

Vanderburg A., Johnson J. A., 2014, PASP, 126, 948

Vaughan A. H., Preston G. W., Wilson O. C., 1978, PASP, 90, 267
Walker J. C. G., 1986, Icarus, 68, 87
Wilson O. C., 1978, ApJ, 226, 379
Winn J. N. et al., 2011, ApJ, 737, L18
Wolfgang A., Rogers L. A., Ford E. B., 2016, ApJ, 825, 19
Yurchenko S. N., Barber R. J., Tennyson J., 2011, MNRAS, 413, 1828
Yurchenko S. N., Tennyson J., 2014, MNRAS, 440, 1649
Zhou G. et al., 2021, AJ, 161, 2
Zhou G. et al., 2022, AJ, 163, 289

[1] *Centre for Astrophysics, University of Southern Queensland, 499-565 West Street, Toowoomba, QLD 4350, Australia*

[2] *SRON, Netherlands Institute for Space Research, Niels Bohrweg 4, NL-2333 CA, Leiden, The Netherlands*

[3] *Center for Astrophysics | Harvard & Smithsonian, 60 Garden Street, Cambridge, MA 02138, USA*

[4] *Winton Fellow*

[5] *Astronomy Unit, Queen Mary University of London, Mile End Road, London E1 4NS, UK*

[6] *Astrophysics Group, Cavendish Laboratory, J.J. Thomson Avenue, Cambridge CB3 0HE, UK*

[7] *Observatoire de Genève, Université de Genève, 51 Chemin Pegasi, CH-1290 Versoix, Switzerland*

[8] *School of Physics & Astronomy, University of Birmingham, Edgbaston, Birmingham B15 2TT, UK*

[9] *Astrophysics Group, Keele University, Keele ST5 5BG, UK*

[10] *Department of Physics and Kavli Institute for Astrophysics and Space Research, Massachusetts Institute of Technology, Cambridge, MA 02139, USA*

[11] *Department of Earth, Atmospheric and Planetary Sciences, Massachusetts Institute of Technology, 77 Massachusetts Ave, Cambridge, MA 02139, USA*

[12] *Department of Aeronautics and Astronautics, Massachusetts Institute of Technology, 77 Massachusetts Avenue, Cambridge, MA 02139, USA*

[13] *Department of Astrophysical Sciences, Princeton University, 4 Ivy Lane, Princeton, NJ 08544, USA*

[14] *NASA Ames Research Center, Moffett Field, CA 94035, USA*

[15] *SETI Institute, Mountain View, CA 94043, USA*

[16] *Instituto de Astrofísica de Canarias, C/ vía Láctea, s/n, E-38205 La Laguna, Tenerife, Spain*

[17] *Departamento de Astrofísica, Universidad de La Laguna (ULL), E-38206 La Laguna, Tenerife, Spain*

[18] *Department of Physics, University of Warwick, Gibbet Hill Road, Coventry CV4 7AL, UK*

[19] *Centre for Exoplanets and Habitability, University of Warwick, Gibbet Hill Road, Coventry CV4 7AL, UK*

[20] *Department of Astronomy, The University of Texas at Austin, TX 78712, USA*

[21] *Department of Earth and Planetary Sciences, University of California, Riverside, CA 92521, USA*

[22] *Department of Physics and Astronomy, University of Louisville, Louisville, KY 40292, USA*

[23] *Department of Physics & Astronomy, George Mason University, 4400 University Drive MS 3F3, Fairfax, VA 22030, USA*

[24] *Shanghai Astronomical Observatory, Chinese Academy of Sciences, Shanghai 200030, China*

This paper has been typeset from a TEX/LATEX file prepared by the author.